Journal of Computational Physics **170,** 812–829 (2001)
doi:10.1006/jcph.2001.6764, available online at http://www.idealibrary.com on IDEAL®

Multiscale Lattice Boltzmann Schemes with Turbulence Modeling

Olga Filippova,*[,1] Sauro Succi,† Francesco Mazzocco,‡ Cinzio Arrighetti,‡ Gino Bella,§ and Dieter Hänel*

*Institute of Combustion and Gasdynamics, University of Duisburg, 47048 Duisburg, Germany; †Institute of Computing Applications, Viale Policlinico 137, CNR Rome, Italy; ‡Mechanics and Aeronautics Department, University of Rome "La Sapienza," Rome, Italy; and §Mechanical Engineering Department, University of Rome "Tor Vergata," Rome, Italy
E-mail: succi@iac.rm.cnr.it

Received June 6, 2000; revised January 3, 2001

The viability of multiscale lattice Boltzmann schemes for the numerical simulation of turbulent flows is discussed and numerically demonstrated for turboaxial machine applications. The extension of boundary-fitting formulas based on wall functions is proposed, which enables the efficient computation of turbulent flows in complex curvilinear geometry using a simple Cartesian grid. Examples of two-dimensional turbulent flows in an axial compressor cascade are presented. © 2001 Academic Press

Key Words: lattice-BGK model; grid refinement.

1. INTRODUCTION

Lattice kinetic theory, and most notably the lattice Boltzmann (LB) method [1, 2] has received considerable interest in the past decade as an efficient method of computing a variety of fluid flows, ranging from low-Reynolds-number flows in porous media to highly turbulent flows [4, 7, 18, 24]. Until recently, LB applications to flows of engineering interest have been held back by a certain lack of flexibility to accommodate nonuniform grids. To circumvent this limitation, a number of variants have been proposed [8, 9], most of which are based on a combination of LB with consolidated finite volume or finite difference techniques. This merge has considerably extended the range of application of the LB method at a fairly reasonable cost in terms of computational complexity. Nonetheless, these merges can accommodate only relatively smooth variations of the flow field because large deformations of the nonuniform mesh may result in numerical instabilities. Many phenomena of

[1] Affiliated with Aerodynamical Institute, RWTH Aachen, Wüllnerstrasse zw. 5 and 7, 52062 Aachen, Germany.

0021-9991/01 $35.00

physical and engineering interest, however, exhibit violent excursions over highly localized regions (boundary layers, shock fronts) which require a correspondingly highly clustered mesh. A powerful response to this kind of need in modern computational fluid dynamics is provided by *unstructured* meshes, namely discrete grids where the number of neighbors of a given node may change from place to place. This allows much stronger distortions of the computational grid, but only at the expense of a significantly more complex data structure. Another popular possibility is provided by *locally embedded* grids, namely, grids in which the local connectivity (number of neighbors) is unchanged but the lattice spacing is refined or coarsened locally, typically in steps of two for practical purposes. Local embedding is a specific instance of a more general framework known as *multiscale algorithms*.

Multiscale LBE schemes were proposed in [14], and subsequently tested and validated for moderate Reynolds number flows around cylinders and blades [14–16].

In this paper we demonstrate the viability of the multiscale LBE scheme for turbulent flows in complex curvilinear geometry, namely, two-dimensional flows in an axial compressor cascade.

2. BASICS OF THE MULTISCALE LB METHOD

Our starting point is the lattice BGK formulation of fluid dynamics [3]:

$$f_i(\mathbf{r} + \mathbf{C}_i\delta t, t + \delta t) - f_i(\mathbf{r}, t) = -\omega\big[f_i(\mathbf{r}, t) - f_i^{\mathrm{eq}}(\mathbf{r}, t)\big]. \tag{1}$$

Since this equation has been described at length in many papers, only essential information shall be provided below.

Here f_i is a set of discrete populations representing the number density of particles at position $\mathbf{r}$ at time t moving along the direction identified by the discrete speed $\mathbf{C}_i$. For "isothermal" LBGK schemes [3] all moving molecules have the same Cartesian speed component $C = \delta_x/\delta_t$, where δ_x is the lattice spacing of the grid.

The right-hand side of (1) represents the relaxation to a local equilibrium f_i^{eq} in a time lapse $\delta t\omega^{-1}$. Here we will use the expression for equilibrium distribution function proposed in [17] for simulation of incompressible flows with constant density $\rho_0 = 1$. Once the discrete populations are known, fluid pressure and speed are obtained by (weighted) sums over the set of discrete speeds:

$$P = \frac{\rho_0 C^2}{3}\sum_i f_i, \qquad \mathbf{U} = \sum_i f_i\mathbf{C}_i. \tag{2}$$

The multiscale implementation of the LB method is based on the following steps. Grid refinement is performed by dividing the lattice spacing by a refinement factor n. The kinematic viscosity, defined in the frame of the LBGK model, depends on the lattice spacing as follows:

$$\nu = \frac{\delta_x C}{6}\left(\frac{2}{\omega} - 1\right).$$

To achieve the same viscosity, hence the same Reynolds number on the coarse and fine

grids, the relaxation parameter in LBGK scheme must be rescaled as

$$\omega_f = \frac{2}{1 + n\left(\frac{2}{\omega_c} - 1\right)}, \tag{3}$$

where ω_f and ω_c are relaxation parameters on the fine and coarse grid respectively and n is the parameter of refinement. The discrete distribution function can be split into an equilibrium and nonequilibrium components:

$$f_i = f_i^{\text{eq}} + f_i^{\text{neq}}. \tag{4}$$

Using LBGK equation, the nonequilibrium component can be obtained as

$$f_i^{\text{neq}} = -\frac{\delta_t}{\omega}[\partial_t + C_{i\alpha}\partial_\alpha] f_i^{\text{eq}} + O(Kn^2), \tag{5}$$

which is second-order accurate in the Knudsen number $Kn = \delta_x/L$, where L is a typical macroscopic scale of the flow on the grid with lattice spacing δ_x.

It is important to realize that this scale can change significantly from place to place in the flow and the task of the multiscale procedure is precisely to adapt the grid resolution to this change of scales.

Knudsen numbers, different for the grids with different lattice spacings, must be of the same order in the whole computational domain.

In the low-frequency limit $\delta_t/T \sim Kn^2$ (see details in [16]), the nonequilibrium component of the distribution function simplifies to

$$f_i^{\text{neq}} = -\frac{\delta_t}{\omega} C_{i\alpha}\partial_\alpha f_i^{\text{eq}} + O(Kn^2). \tag{6}$$

Combining the above relation with continuity of the hydrodynamic variables and their derivatives at the interface between the two grids delivers the relation between the coarse and fine grid populations,

$$f_i' = \tilde{F}_i^{\text{eq}} + \left(\tilde{F}_i' - \tilde{F}_i^{\text{eq}}\right)\Omega^{-1}, \quad F_i' = f_i^{\text{eq}} + \left(f_i' - f_i^{\text{eq}}\right)\Omega, \tag{7}$$

where capital means coarse grid, prime means postcollision, tilde stands for interpolation from the coarse grid, and $\Omega = n((1-\omega_c)\omega_f/(1-\omega_f)\omega_c)$. The relation (7) defines a map between coarse and fine grids which clearly reduces to the identity in the limit $n \to 1$.

The final one-step algorithm reads as follows:

1. *Move and Collide F*
2. *For all subcycles* $k = 0, 1, \ldots, n-1$ *do:*
   a. *Interpolate F on the interface coarse-to-fine grid*
   b. *Scale F to f via 7 on the interface coarse-to-fine grid*
   c. *Move and Collide f*
3. *End do*
4. *Scale back f to F via 7 on the interface fine-to-coarse grid.*

For steady-state flows this algorithm can be accelerated by use of only one subcycle in step 2 [16].

3. TURBULENCE MODELING

The main benefit of the grid-refined LBGK scheme is a better resolution in the regions of high gradients where turbulence is produced. Nonetheless, grid refinement alone is not able to reach high Reynolds numbers, namely $Re \geq 10^5$. As a result, some form of turbulence modeling is needed.

Two-equation models for turbulence, and among them k–ϵ models, remain the most popular choice for the simulation of turbulent flows. Previously it was suggested [6] that the k–ϵ equations be solved within an LB structure by creating two additional populations, with components in the same directions as the particle distribution, for each of the turbulent properties which are defined as kinetic moments of the corresponding populations. Another approach using LB in conjunction with finite difference schemes for the solution of k–ϵ equations was proposed in [18] based on the algorithm developed in [19].

At the same time, similar kinds of combined LBGK–finite difference schemes have been successfully developed for the problems of low-Mach-number combustion [12, 13]. In both cases LB schemes are "responsible" for the solution of continuity and momentum equations, whereas convective–diffusion equations with source terms in both systems of equations are solved with finite difference schemes using different numerical methods.

Here this combined approach is extended to the multiscale framework. The two-equation model for turbulent kinetic energy k and dissipation ϵ reads

$$\rho_0 \frac{\partial k}{\partial t} + \rho_0 U_\alpha \frac{\partial k}{\partial x_\alpha} = \frac{\partial}{\partial x_\alpha}\left(\left(\frac{\mu_0}{\sigma_{k0}} + \frac{\mu_T}{\sigma_{kT}}\right)\frac{\partial k}{\partial x_\alpha}\right) + \tau_{\alpha\beta} S_{\alpha\beta} - \rho_0 \epsilon \tag{8}$$

$$\rho_0 \frac{\partial \epsilon}{\partial t} + \rho_0 U_\alpha \frac{\partial \epsilon}{\partial x_\alpha} = \frac{\partial}{\partial x_\alpha}\left(\left(\frac{\mu_0}{\sigma_{\epsilon 0}} + \frac{\mu_T}{\sigma_{\epsilon T}}\right)\frac{\partial \epsilon}{\partial x_\alpha}\right) + C_{\epsilon 1}\frac{\epsilon}{k}\tau_{\alpha\beta} S_{\alpha\beta} - \left(C_{\epsilon 2} + f_{RNG} C_\mu \frac{\theta^3(1-\theta/\theta_0)}{1+\beta\theta^3}\right)\rho_0 \frac{\epsilon^2}{k}, \quad \mu_T = \rho_0 C_\mu \frac{k^2}{\epsilon}, \tag{9}$$

where θ is a dimensionless shear rate, $\theta = |S|k/\epsilon$, $|S| = (2S_{\alpha\beta}S_{\alpha\beta})^{1/2}$,

$$\tau_{\alpha\beta} = 2\mu_T S_{\alpha\beta} - \frac{2}{3}\rho_0 k \delta_{\alpha\beta}$$

is the stress tensor, and $S_{\alpha\beta}$ is the strain-rate tensor $S_{\alpha\beta} = \frac{1}{2}(\frac{\partial U_\beta}{\partial x_\alpha} + \frac{\partial U_\alpha}{\partial x_\beta})$. In the low-frequency limit, the strain-rate tensor can be obtained with accuracy $O(Kn^2)$ as a second-order moment of the nonequilibrium distribution function:

$$S_{\alpha\beta} = -1.5\omega \sum_i \left(f_i - f_i^{\text{eq}}\right) C_{i\alpha} C_{i\beta}/C^2 \cdot \frac{C}{\delta_x}.$$

The values of the closure coefficients for the standard k–ϵ and k–ϵ RNG models can be found in [20, 21].

The system of equations (8) and (9) can be rewritten in dimensionless variables,

$$\bar{k} = \frac{k}{C^2}, \quad \bar{\epsilon} = \frac{\epsilon \delta_x}{C^3}, \quad \bar{x} = \frac{x}{L}, \quad \bar{t} = \frac{tC}{L},$$

$$M = \frac{U}{C}, \quad \bar{S}_{\alpha\beta} = -1.5\omega \sum_i \left(f_i - f_i^{\text{eq}}\right) C_{i\alpha} C_{i\beta}/C^2.$$

In the low-frequency limit one can obtain from the lattice BGK equation (Eq. (1)) the following relationship between dimensionless strain rate tensors on the fine and coarse grids, respectively:

$$\bar{S}^f_{\alpha\beta} = \bar{S}^c_{\alpha\beta}/n.$$

Upon considering the system of dimensionless equations for $\bar{k}$ and $\bar{\epsilon}$ on the fine and coarse grids, one obtains that the left-hand side of both dimensionless equations (after multiplication of the equation for dissipation on the fine grid by the parameter of refinement n) are not changed, whereas the source terms on the fine grid are reduced compared with the source terms on the coarse grid, because of the following scaling relationships:

$$\bar{\epsilon}^f = \bar{\epsilon}^c/n, \quad \left(\frac{\bar{k}^2}{\bar{\epsilon}}\bar{S}_{\alpha\beta}\bar{S}_{\alpha\beta}\right)^f = \left(\frac{\bar{k}^2}{\bar{\epsilon}}\bar{S}_{\alpha\beta}\bar{S}_{\alpha\beta}\right)^c \Big/ n.$$

The equations for $\bar{k}$ and $\bar{\epsilon}$ are solved on the same grids as LBGK equations using a standard explicit time marching of central difference scheme for all spatial derivatives of variables $\bar{k}$ and $\bar{\epsilon}$. The LBGK equations (Eq. (1)) and equations for $\bar{k}$ and $\bar{\epsilon}$ are considered to be decoupled during a single time step. At the new time level t the values of dimensionless eddy viscosity $\mu_T(\mathbf{r}, t)/(\rho_0\delta_x C)$ computed via the new values of $\bar{k}(\mathbf{r}, t)$ and $\bar{\epsilon}(\mathbf{r}, t)$ are used for the recalculation of the relaxation parameter $\omega(\mathbf{r}, t)$ in the LBGK scheme (Eq. (1)). The lower thresholds for $\bar{k}$ and $\bar{\epsilon}(\bar{k} = \bar{k}_{inlet} = 10^{-6}$–$10^{-5}, \bar{\epsilon} = \bar{\epsilon}_{inlet} = 7 \times 10^{-9})$ used in our computations validating the code stabilize essentially this scheme.

3.1. *LBGK Scheme in the Inviscid Flow Limit*

In the low-frequency limit, the pressure and velocity fields obtained from the numerical LBGK simulations as moments of distribution functions (Eq. (2)) satisfy the Navier–Stokes equations for incompressible flows with second-order accuracy in the Knudsen number.

High-frequency components usually introduced in the LBGK scheme by initial conditions dissipate rather quickly in the transitional stage of computations for moderate Reynolds number flows if no high-frequency disturbances are generated or amplified by boundary conditions. Once this dissipation takes place, the subsequent time evolution of the LBGK scheme reproduces only the low-frequency, hydrodynamic solution . The problem in LBGK simulations of high-Reynolds-number flows (and, in fact, of *any* numerical fluid solver) is that the dissipation of high-frequency components becomes very small.

Below we analyze the question of whether it is possible to use an artificial value of kinematic viscosity without impairing the accuracy of the solution for high-Reynolds-number flows. The kinematic viscosity ν in fluid dynamic simulations with the LBGK scheme is related to the relaxation parameter ω by the expression

$$\nu = \frac{\delta_x C}{6}\left(\frac{2}{\omega} - 1\right).$$

Substituting it in the definition of Reynolds number, we obtain

$$Re = \frac{6U_0L_0}{\delta_x C\left(\frac{2}{\omega} - 1\right)},$$

from which we see that with $Re \to \infty$ the relaxation parameter in the LBGK equation (Eq. (1)) tends to the value 2.

Expansion of LBGK equation in Taylor series with respect to small parameter $\delta_x = C\delta_t$ (small related to characteristic length of the flow) for steady-state flows reads

$$\delta_x \frac{\partial f_i}{\partial x_\alpha} c_{i\alpha} + \frac{\delta_x^2}{2} \frac{\partial^2 f_i}{\partial x_\alpha \partial x_\beta} c_{i\alpha} c_{i\beta} + \omega\left(f_i - f_i^{\text{eq}}\right) = O(Kn^3), \quad c_{i\alpha} = \frac{C_{i\alpha}}{C}. \tag{10}$$

The macroscopic momentum equation is obtained from the first part of Eq. (10) by splitting the distribution function f_i into an equilibrium and a nonequilibrium part (Eqs. (4) and (5)) and using the equation of continuity:

$$\delta_x \partial_\beta \left(U_\alpha U_\beta + \frac{P}{\rho_0} \delta_{\alpha\beta} \right) = \delta_x \partial_\beta \nu \partial_\beta U_\alpha + O(Kn^3). \tag{11}$$

Using the equation of continuity and usual estimate of spatial derivatives,

$$\delta_x \frac{\partial F}{\partial x} \sim \frac{\delta_x}{L}[F]^s = Kn[F]^s, \quad \delta_x^2 \frac{\partial^2 F}{\partial x^2} \sim \frac{\delta_x^2}{L^2}[F]^s = Kn^2[F]^s,$$

where $[F]^s$ denotes the local deviation of variable F on the characteristic length L, one can see that the orders of advective and viscous terms in the momentum equation are given, respectively, by

$$U[U]^s Kn, \quad \frac{[U]^s C Kn^2}{6}\left(\frac{2}{\omega} - 1\right), \tag{12}$$

where U is the value of local velocity.

According to the definition of Reynolds number, in the inviscid flow limit we have $\omega \to 2$. But from the estimations (12), we also observe that ω can be taken arbitrarily in the range $\omega \sim O(\frac{2}{1+6KnU/C})$.

Then, the ratio between viscous and advective term in Eq. (11) becomes $O(Kn^2)$ and Eq. (11) results in the Euler equation, with second-order accuracy in the Knudsen number.

To ensure a fixed accuracy of the order Kn^2, the relaxation parameter ω has to acquire a dependence on the local Mach number U/C (at least in the regions where local Mach numbers are an order of magnitude smaller than the global Mach number U_0/C).

In our computations, this dependence was not taken into account. We have used a fixed artificial value of ω such that $\omega \sim 2 - O(Kn)$. This can locally decrease the accuracy of solution in the narrow vicinity of stagnation points. In the other regions of the flow with $U/C \sim U_0/C \sim Kn \sim 0.1$ this relaxation parameter corresponding to the value of artificial viscosity $O(\frac{Kn}{12})$ does not change the second-order accuracy of the solution.

We also emphasize that because the artificial relaxation parameter ω does not represent the real viscosity, it does not have to be rescaled according to Eq. (3) in the transition between two grids with the different lattice spacings. For any grid it can be chosen arbitrarily in the limits discussed above.

3.2. *Boundary-Fitting Formulation for Wall Functions*

Different ways of realizing wall function formulations were used recently in lattice Botzmann schemes incorporating turbulence models [18, 23]. Here we are dealing with the boundary-fitting formulation proposed in [10].

The boundary-fitting formulation for no-slip conditions was derived as a weighted combination of bouncing-back and the "equilibrium state conditions" with adjusting parameters depending on the location of the curvilinear boundary between the nodes of the basic LBGK equidistant Cartesian grid. Completed with the additional term, first introduced in the bouncing-back formula by Ladd [11], the boundary-fitting formulation is able to describe Dirichlet boundary conditions for velocity on arbitrary curvilinear boundaries in the low-frequency limit. The theoretical estimation that the boundary-fitting formulation does not decrease the second-order accuracy of the outer scheme if applied to an arbitrary curvilinear boundary was given in [10, 14]. It was also numerically confirmed in [16] using Richardson's formula.

The extension of this formulation to the case of slip conditions and wall functions is proposed. In the former case, the fluid speed at the crossing points of the boundary and links of the grid are linearly extrapolated at every time step along the normal from the outer flow. This makes it possible to simulate inviscid flows in complex geometry.

In the case of turbulent flow simulation, the fluid speed in the logarithmic part of turbulent boundary layer reads

$$\frac{u_\tau}{U_s} = \frac{1}{\kappa}\ln(y^+) + B, \quad y^+ = \frac{U_s y}{\nu}, \tag{13}$$

where u_τ is the mean velocity parallel to the wall, κ is the von Karman constant ($\kappa = 0.41$), B is an empirical constant related to the thickness of the viscous sublayer ($B = 5$ in our simulations), ν is the molecular viscosity, U_s is the shear stress velocity $U_s^2 = \tau_w/\rho_0$, τ_w is the shear stress at the wall, and y^+ is the dimensionless distance from the boundary. For the logarithmic region of turbulent boundary layer, y^+ lies typically between 30 and 500 and, as one can see from Eq. (13), for $Re \to \infty$, $y : (30 < y^+ < 500) \to 0$. For this case, a boundary-fitting formulation allowing description of the Dirichlet boundary condition for velocity on a line (in 2D) or a surface (in 3D) not aligned with the numerical grid becomes crucial.

The surface L lying inside the logarithmic region of the turbulent boundary layer on which Eq. (13) is valid is sketched in Fig. 1. The distances to the surface L along the crossing links i from the neighbouring "fluid" nodes, components of normal vector to the boundary of the body $\mathbf{n}$ in the crossing points $\mathbf{r}_{c,}$ and distances from the crossing points $\mathbf{r}_c$ to the boundary of the body h_c are computed at the onset once. At time level t^n the normal to the vector $\mathbf{n}$ velocity in the point $\mathbf{r}_c$, $\mathbf{u}_\tau$, is linearly extrapolated from the outer flow. The shear stress velocity U_s^n is found from Eq. (13) using Newton's method. To avoid numerical instability the relaxation to Eq. (13) is used in the computations.

Under the assumption that the flow is in local equilibrium (meaning that the production and dissipation are nearly equal), the shear stress velocity reads

$$U_s = C_\mu^{1/4}\sqrt{k}_0.$$

The value of k_0^n on the boundary of the body then is obtained as

$$k_0^n = \left(U_s^n\right)^2 / \sqrt{C}_\mu.$$

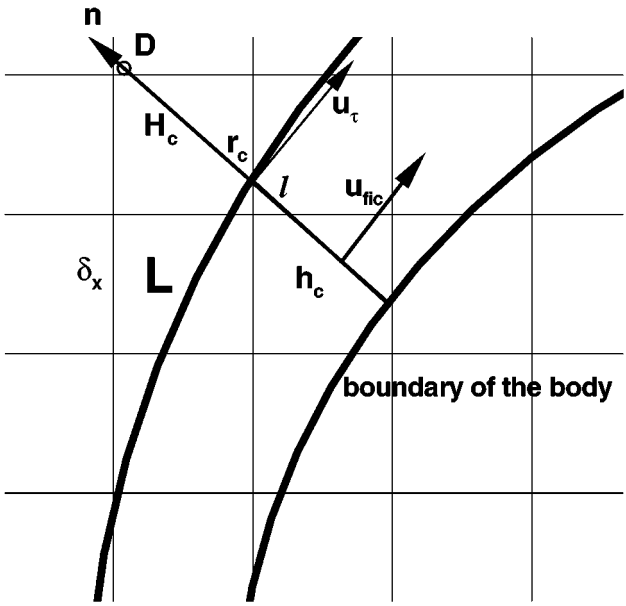

FIG. 1. Computational mesh and geometrical relations for wall functions formulations.

The value of k_c in the point $\mathbf{r}_c$ is obtained as

$$k_c = \left(k^n(\mathbf{r}_D) - k_0^n\right)\frac{h_c^2}{(h_c + H_c)^2} + k_0^n$$

(parabolic fit with $\partial k/\partial n = 0$ on the boundary of the body). The value of $k^n(\mathbf{r}D)$ in the point D: $\mathbf{r}_D = \mathbf{r}_c + H_c\mathbf{n}$ is interpolated with Bessel formula from the value of k^n in the nodes of computational mesh.

The value of ϵ_c^n reads

$$\epsilon_c^n = \frac{C_\mu^{3/4} k_c^{3/2}}{\kappa h_c}.$$

These values are used to evaluate spatial derivatives of k and ϵ at time t^n in the neighboring nodes to the surface L. Using the value of tangential velocity in the point $\mathbf{r}_c$ in the boundary-fitting formula [10], as linearly interpolated from the values $\mathbf{u}_D^n$ and fictitious velocity $\mathbf{u}_{fic}^n$ computed at the point $\mathbf{r}_c - l\mathbf{n}$, $l = O(\delta_x)$ according to the law of wall

$$u_{fic}^n = u_\tau^n - U^s l/(\kappa h_c), \tag{14}$$

one can move to the next time level t^{n+1}. In the low-frequency limit the LBGK scheme with turbulence modeling using these boundary conditions provides macroscopically the solution of RANS Navier–Stokes equations smoothly connected on the surface L with the logarithmic law of wall in the region between the surface L and the surface of the body.

Similarly, the boundary-fitting formulation can be applied in viscous and buffer sublayers. The universal dependence $u^+ = f(y^+)$ in the turbulent boundary layer is important. It enables us to compute derivatives of the tangential component of velocity along the normal in the point $\mathbf{r}_c$ and accordingly, the value of the fictitious velocity $\mathbf{u}_{fic}^n$ at any distance

$l \sim O(\delta_x)$ along the normal toward the wall. The value of the velocity in the point $\mathbf{r}_c$ in the boundary-fitting formulas is obtained using linear interpolation of the stream velocity $\mathbf{u}_D^n$ and fictitious velocity $\mathbf{u}_{fic}^n$.

We emphasize that general formulas such as Eq. (13) are strictly valid only for turbulent flow over a flat plate. Their application to turbulent flows around arbitrary curvilinear boundaries requires in some cases local refinement of the coarse grid such that the boundary can be locally treated as a flat plate.

4. RESULTS

4.1. *Validation of the Code*

To validate the code and to estimate its computational performance, the flow around a NACA 4412 profile with small angles of attack is considered. Two different k–ϵ models, the k–ϵ RNG and the standard k–ϵ, are used and compared with experiments based on the data from [26].

The computational experiment is as follows: For the angle $\alpha = -0.5^\circ$ the flow is injected at the inlet and upper section of the computational domain with an LBGK Mach number of $U_{in}/C = 0.08$. For the angle $\alpha = 2.9^\circ$ the flow is injected at the inlet and lower section of the computational domain at a LBGK Mach number $U_{in}/C = 0.08$. The other kind of boundary condition used in the numerical simulations at the "injection" section of the computational domain is the extrapolation of x component of the velocity from the outer flow and the constant inclination α of the stream. Pressure at inlet and "injection" sections is extrapolated along the normal to the section from the outer flow. Pressure at outlet is assumed to be constant. At outlet the velocity is extrapolated along the normal from the outer flow; at the other "outlet" section the x component of velocity is also extrapolated along the normal from the outer flow whereas the normal component of velocity is obtained under the condition of constant inclination α of the stream. Pressure at this section is defined according to the Bernoulli equation.

Two values of the Reynolds numbers related to the length of the chord were considered, $Re = 10^6$ and $Re = 3 \times 10^6$; in [26] the value of Reynolds number was not defined precisely (approximately 3,000,000). The computational domain consists of 160×111 nodes.

Grid refinement defined by the parameter $n = \delta_x^c/\delta_x^f$ is applied to a box $(65\delta_x^c, 17\delta_x^c)$ surrounding the profile with the left-down corner at (40 and 49). The convergence criterion is prescribed as $\max|u(t, \mathbf{r}) - u(t-1, \mathbf{r})| + |v(t, \mathbf{r}) - v(t-1, \mathbf{r})| < 1 \times 10^{-6}$ in the nodes of the coarse grid. The accelerated scheme using one time step on the fine grid versus one time step on the coarse grid is used. The value of ω_{coarse} in the absence of turbulent viscosity is 1.95 for the simulations with the k–ϵ RNG model and 1.92 for the simulations with the standard k–ϵ model.

We emphasize that in the law-of-wall formulation (Eq. (13)) the molecular viscosity $\nu = Re/(U_0 L_0)$ must be used.

The relative positions of the surface L due to the displacement of wall layer with respect to the surface of airfoil are shown in Fig. 2a for the particular case $Re = 10^6, \alpha = 2.9^\circ$. The main results for the k–ϵ RNG model are collected in Figs. 2b and 2c and for the standard k–ϵ model in Figs. 3a and 3b where the numerically and experimentally obtained pressure coefficients along a chord of profile are shown for different angles of attack. Parameter of refinement in the numerical simulations was taken as $n = 5$. In addition, the numerical results for $Re = 10^6$ and $n = 3$ are shown in Fig. 2c with dotted lines.

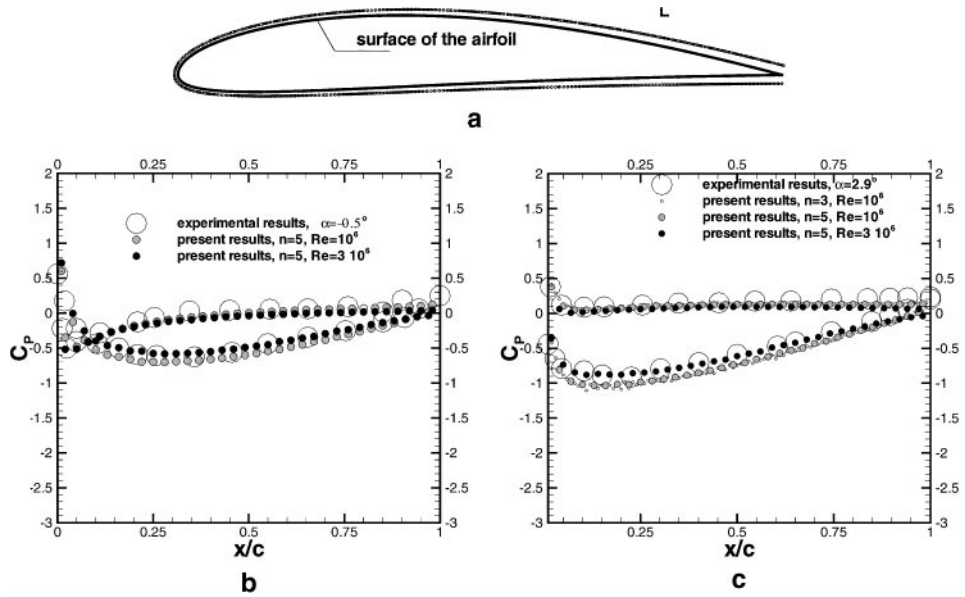

FIG. 2. (a) Relative positions of the surface L and the surface of the airfoil in the numerical simulation of the turbulent flow around NACA 4412 profile at $Re = 10^6$, $\alpha = 2.9^\circ$. (b) Pressure coefficient C_P along the chord of the NACA 4412 profile, $\alpha = -0.5^\circ$. Solid circles represent present solution, k–ϵ RNG model, open circles represent experimental results [25, 26]. (c) Pressure coefficient C_P along the chord of the NACA 4412 profile, $\alpha = 2.9^\circ$. Solid circles represent present solution, k–ϵ RNG model, open circles represent experimental results [25, 26].

As one can see from Figs. 2b, 2c, 3a, and 3b that both C_P curves for $Re = 10^6$ and $Re = 3 \times 10^6$ coincide closely. The change in the boundary conditions at the "injection" section of the computational domain has shown virtually no influence on the pressure distribution on the surface of the airfoil. The agreement between experimental and numerical results is found to be good for both turbulence models.

An important remark is in order. In general, the law of wall can be applied on any surface lying inside the logarithmic part of turbulent boundary layer. In high-Reynolds-number flows, the thickness of the logarithmic part of turbulent boundary layer may become even smaller than the lattice spacing of the fine grid, if the latter is defined *a priori*. Then, the procedure described above loses the right resolution of the velocity field in the "rest" of the logarithmic part of turbulent boundary layer, lying above the surface L. This may cause deviations of the pressure field from the right values.

To avoid this effect one has to use finer resolution around the surface L or, what is more effective and enables the use of coarser grids, to adapt the position of the surface L to the position $y^+ = y^{+,up}$ ($y^{+,up} = 500$ in our computations). The best agreement with experimental data [26] in our computations is achieved when y^+ lies in the band (300,500) for ~97% of the chord of airfoil (except the narrow vicinity of the leading edge).

We emphasize that grid refinement together with boundary-fitting formulation for wall functions proves instrumental to ensure good agreement between experimental results and numerical results for turbulent flow simulation around blunt bodies at high Reynolds numbers. As one can see from Table I, the higher quality provided by grid refinement comes at a reasonable cost in CPU and memory requirements. The computations were performed on PC AMD-K7, 500 MHz.

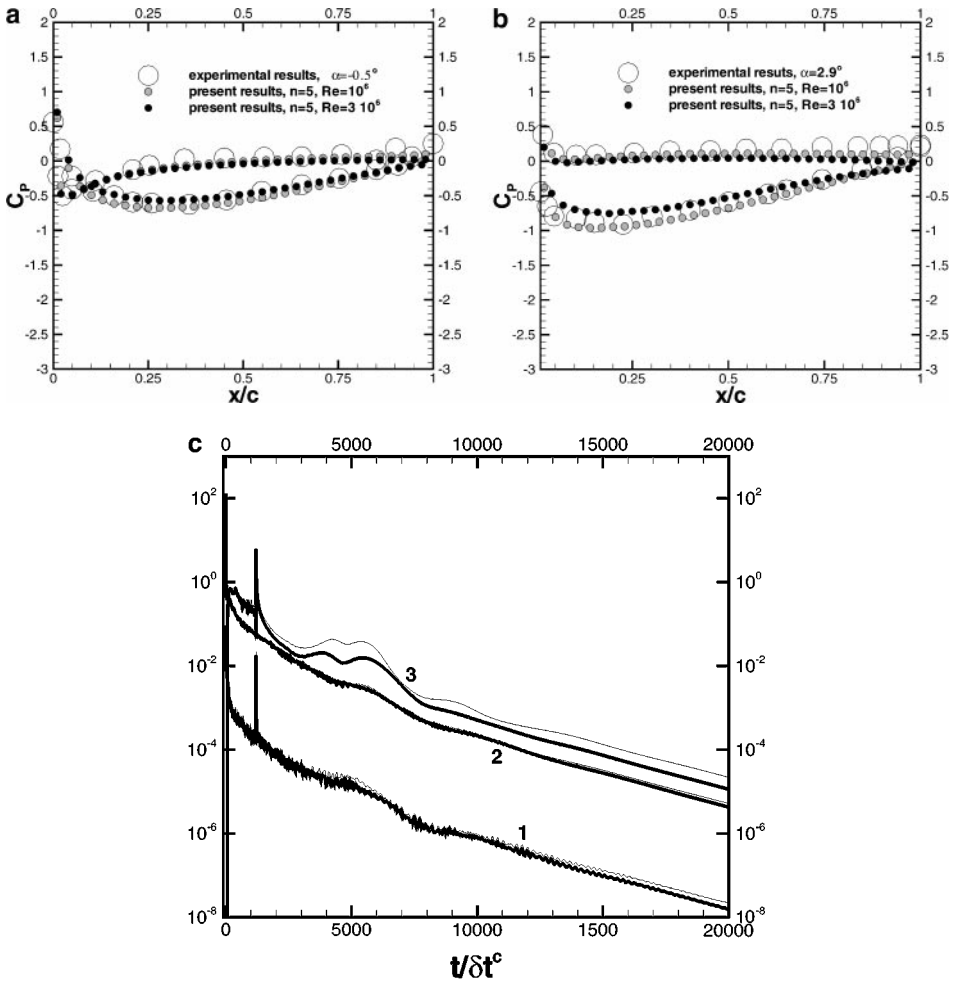

FIG. 3. (a) Pressure coefficient C_P along the chord of the NACA 4412 profile, $\alpha = -0.5^\circ$. Solid circles represent present solution, standard k–ϵ model, open circles represent experimental results [25, 26]. (b) Pressure coefficient C_P along the chord of the NACA 4412 profile, $\alpha = 2.9^\circ$. Solid circles represent present solution, standard k–ϵ model, open circles represent experimental results [25, 26]. (c) Time history of the different errors obtained in the numerical simulations of the flow around NACA 4412 profile, $Re = 10^6$, $\alpha = 2.9^\circ$, Standard k–ϵ model. Bold lines correspond to the case $\omega_{fine} = 1.66$, thin lines to $\omega_{fine} = 1.8$ (here ω_{fine} is the relaxation parameter on the fine grid in the absence of turbulent viscosity). (1) $\max|u(\mathbf{r}, t) - u(\mathbf{r}, t-1)| + |v(\mathbf{r}, t) - v(\mathbf{r}, t-1)|$; (2) $[\sum((u(\mathbf{r}, t) - u(\mathbf{r}, t-1))^2 + (v(\mathbf{r}, t) - v(\mathbf{r}, t-1))^2)]^{0.5}/U_{in}$; (3) $[\sum(k(\mathbf{r}, t) - k(\mathbf{r}, t-1))^2]^{0.5}/k_{in}$.

The temporal behavior of the errors, $\max|u(\mathbf{r}, t) - u(\mathbf{r}, t-1)| + |v(\mathbf{r}, t) - v(\mathbf{r}, t)|$, $[\sum(u(\mathbf{r}, t) - u(\mathbf{r}, t-1))^2 + (v(\mathbf{r}, t) - v(\mathbf{r}, t-1))^2]^{0.5}/U_{in}$, and $[\sum(k(\mathbf{r}, t) - k(\mathbf{r}, t-1))^2]^{0.5}/k_{in}$, is shown in Fig. 3c for $Re = 10^6, \alpha = 2.9^o$ and two different ω_{fine} corresponding to the artificial viscosity on the fine grid: $\omega_{fine} = 1.66$ and $\omega_{fine} = 1.8$. Peaks on all curves correspond to the "switch-on" of the boundary-fitting conditions for wall functions formulation which were not used at the initial (relaxation) stage of the computations. Although k–ϵ equations were solved with the same time stepping as LBGK equations, they are found to take only 18% of the CPU time. This is basically in line with the fact that the turbulence model evolves two scalar fields while LBGK involves nine.

TABLE I
Turbulent Flow around NACA 4412 Profile at the Angle of Attack 2.9°

Re	Model	n	ω_{fine}	Memory requirement	CPU time (s)
10^6	RNG	3	1.86	17.9	1195
10^6	RNG	5	1.77	31.1	2655
3×10^6	RNG	5	1.77	31.1	2676
10^6	Standard	5	1.66	31.1	2208
3×10^6	Standard	5	1.66	31.1	2262

Note. Reynolds number, k–ϵ turbulence model, spatial refinement factor n, relaxation parameter on the fine grid in the absence of turbulent viscosity ω_{fine}, memory usage of the optimized code Mbyte, CPU time in seconds.

In addition, the field of generalized pressure $3(\overline{p} + \frac{2}{3}\overline{k})$ with streamlines in the whole computational domain is shown in Fig. 4 for the case $Re = 10^6, \alpha = 2.9^\circ$ and parameter of refinement 5, using the standard k–ϵ model.

To demonstrate more clearly the loss of the right resolution in the turbulent boundary layer due to the coarsening of the grids and increasing of the Reynolds number, we apply our code to the following simple geometry modeling the flow over the flat plate. The computational domain consists of (N_x, N_y) nodes. In our computations $N_x = 11$, $N_y = 51, 151, 251$. The periodicity in the x direction is imposed on the solution. At the upper section of the computational domain the velocity is extrapolated with the zeroth order from the computational domain, at the lower section boundary-fitting formulas for wall functions with $y^+ = y_0$, $30 \le y_0 \le 500$ are applied. This corresponds to the flat plate lying outside the computational domain parallel to x axis. The characteristic length and velocity used in the definition of the Reynolds number $Re_{sim} = 1000, 5000$ correspond to the lattice

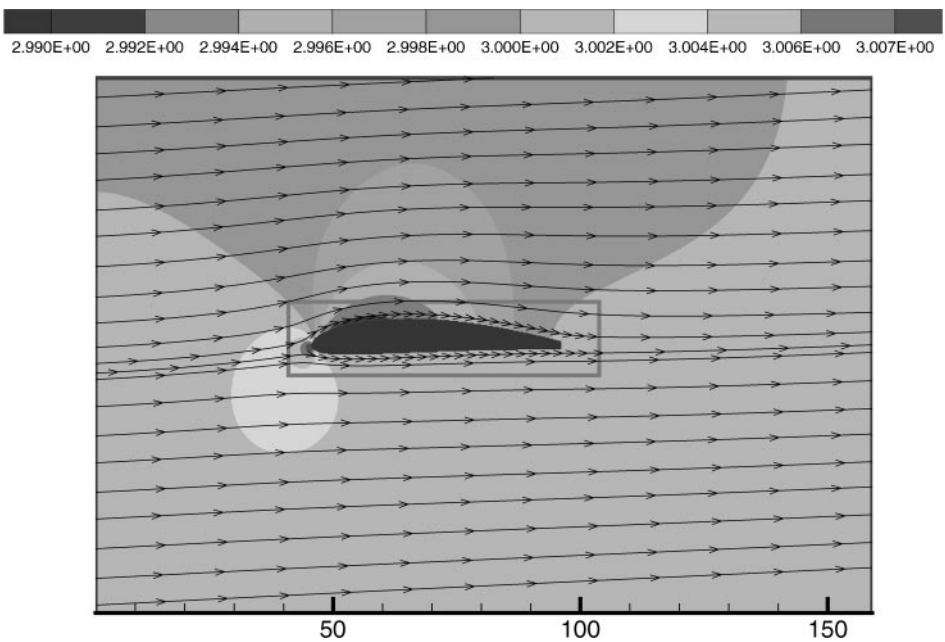

FIG. 4. Turbulent flow around NACA 4412 profile at $Re = 10^6, \alpha = 2.9^\circ$ computed with standard k–ϵ model, parameter of refinement 5. Pressure and streamlines in the whole computational domain.

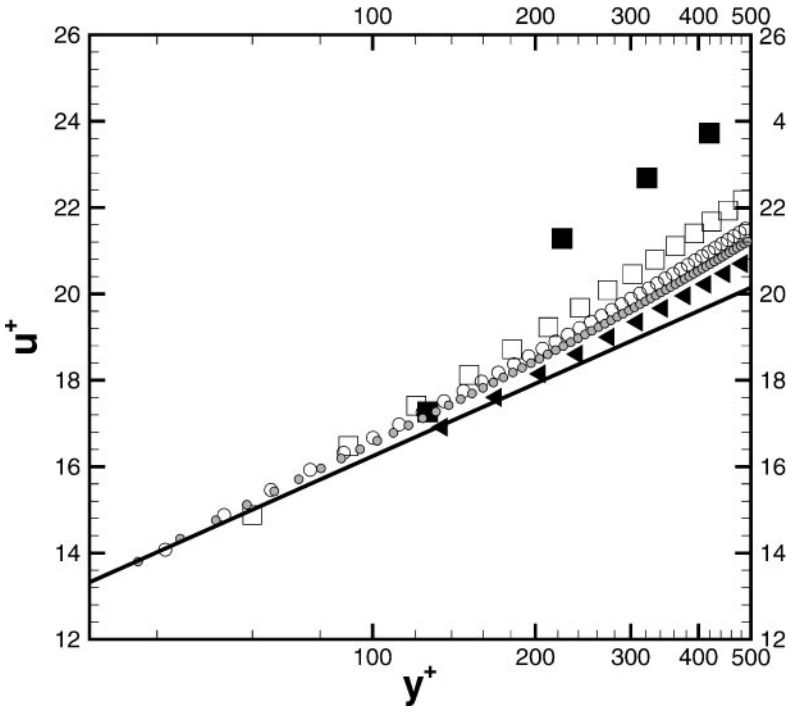

FIG. 5. The part of the turbulent boundary layer $u^+(y^+)$ in the flow over a flat plate resolved on the grids with different densities at different Reynolds numbers Re_{sim}. Solid squares represent the data obtained on the grid with $N_y = 51$, $y_0 = 30$, and $Re_{sim} = 5000$. For $Re_{sim} = 1000$ and $y_0 = 30$ open squares represent the data obtained on the grid with $N_y = 51$, open circles with $N_y = 151$, and solid circles with $N_y = 251$. Solid triangles represent the data obtained on the grid with $N_y = 51$, $y_0 = 100$ at $Re_{sim} = 1000$. In addition the line representing the logarithmic law of wall is shown.

link of the coarsest lattice and initial value of the velocity $U_0 = 0.15C$. The part of the turbulent boundary layer $u^+(y^+)$, $y_0 \le y^+ \le 500$ at $y_0 = 30$, $Re_{sim} = 1000$ resolved on the grids with different grid densities is shown in Fig. 5.

4.2. *Flow Across a Periodic Array of Compressor Blades*

In this section we present an application of multiscale lattice Boltzmann schemes to the case of a two-dimensional flow across a periodic array of compressor blades [22]. The surface of the blade in the periodic computational cell is described by

$$f(x) = a_1(x - \sqrt{x}) + a_2(x^2 - \sqrt{x}) + a_3(x^3 - \sqrt{x}),$$

where x is normalized according to the chord length.

The computational experiment is as follows: the flow is injected at the inlet section at a speed U_{in} and injection angle $\alpha = 16^\circ$.

We use the blade profile with the following coefficients for the upper and lower contours [22]:

$$a_{1up} = 0.09054341, \quad a_{2up} = -0.3910232, \quad a_{3up} = 0.08876120,$$
$$a_{1low} = 0.343766, \quad a_{2low} = -0.02828469, \quad a_{3low} = -0.1469358.$$

FIG. 6. Relative positions of the surface L and the surface of the blade.

The computational domain consists of 350 × 81 nodes. Grid refinement defined by parameter $n = \delta_x^c/\delta_x^f$ is applied to a box surrounding the blade. The value of n, the size of the box in the links of the coarse grid δ_x^c, the left-down corner of the box, and the value of velocity at inlet are denoted for any particular case.

We perform three types of simulations:

1. Direct simulation of viscous flow at $Re = 10^4$
(parameter of refinement 6, the size of the box 120 × 22, left-down corner (117,35), $U_{in}/C = 0.07$.)

2. Direct simulation of inviscid flow
(parameter of refinement 2, the size of the box 120 × 27, left-down corner (117,30), $\omega_c = 1.885$, $\omega_f = 1.782$, $U_{in}/C = 0.1$).

3. Simulation of turbulent flow at $Re = 10^5$ (RANS k–ϵ RNG model)
(parameter of refinement 3, the size of the box 130 × 32, left-down corner (112,30), $U_{in}/C = 0.08$)

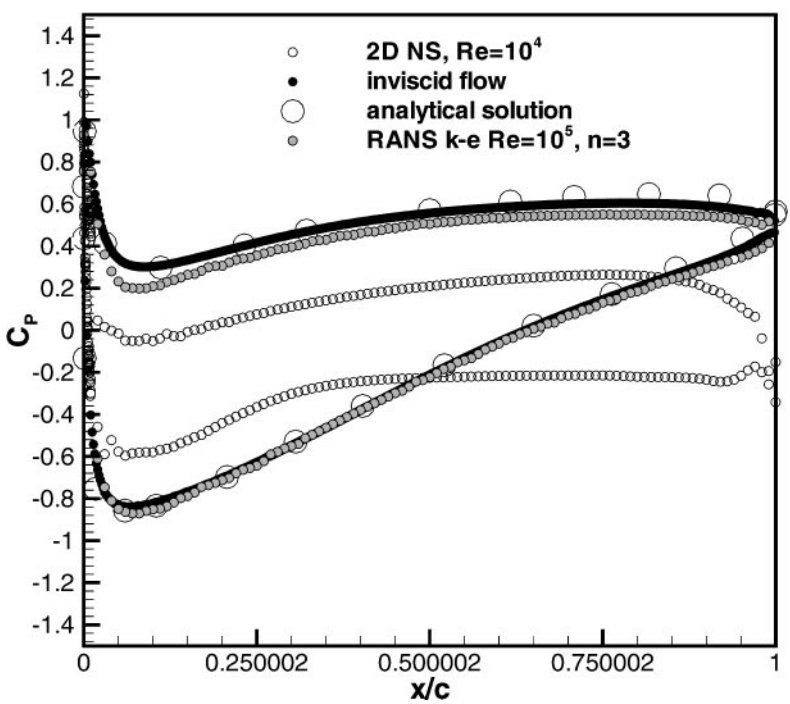

FIG. 7. Pressure coefficient C_P along the chord of the blade for inviscid flow, laminar flow at $Re = 10^4$ (averaged per cycle) and turbulent flows at $Re = 10^5$, $\alpha = 16^\circ$.

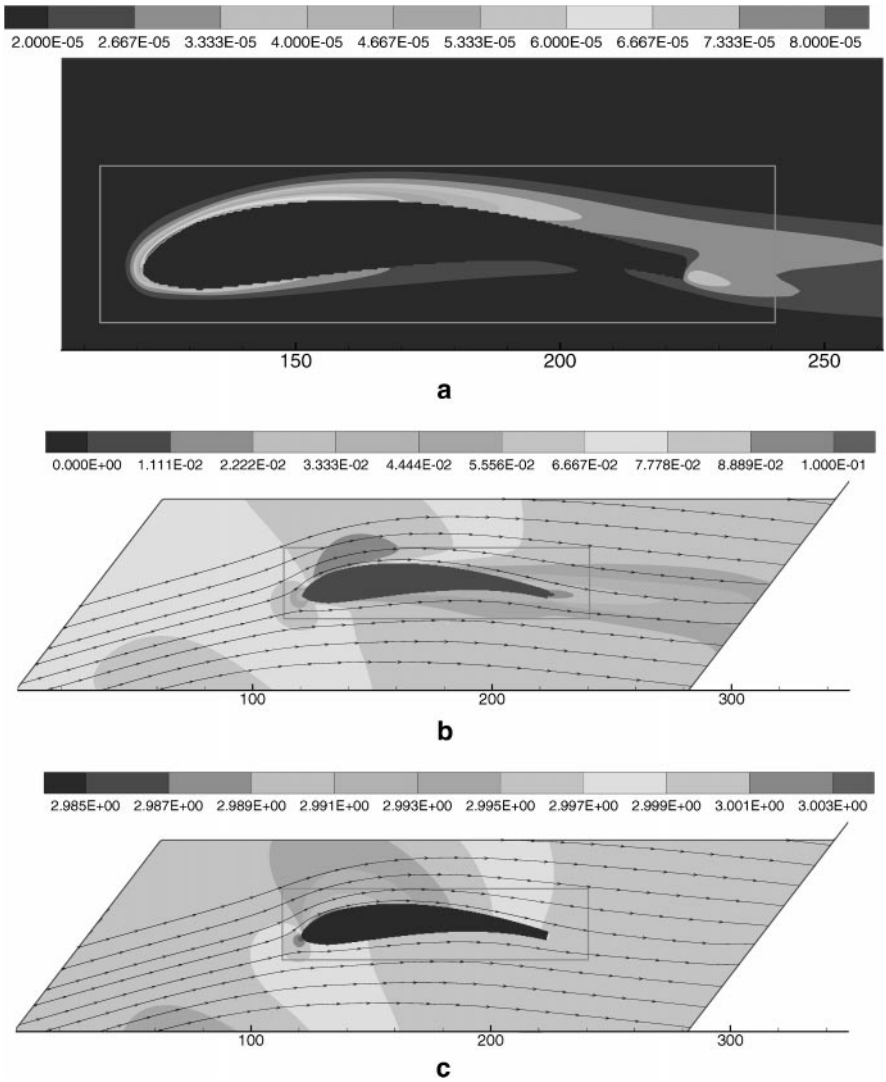

FIG. 8. Turbulent flow in cascade at $Re = 10^5$, $\alpha = 16^\circ$. (a) Turbulent kinetic energy in the vicinity of the blade; (b) x-velocity and streamlines; (c) Generalized pressure and streamlines.

The artificial value of molecular viscosity in turbulent flow simulation corresponds to $\omega_c = 1.92$, $\omega_f = 1.78$. The relative positions of the surface L on which boundary-fitting formulation for wall functions is applied and the surface of the blade are shown in Fig. 6.

The idea is to assess how close we can get to the inviscid results by raising the Reynolds number. The main results are collected in Fig. 7, where the pressure coefficient along a chord are shown for all three cases. From this figure we see that the C_P curve obtained with LBGK scheme using slip conditions in the boundary-fitting formula for inviscid flow simulation is in very good agreement with the analytical solution [22]. The agreement between results for inviscid and turbulent flow at $Re = 10^5$ is also good except the small region in the vicinity of the leading edge. The same discrepancy in the vicinity of leading edge between numerical results for potential flow and experimental data [26] for NACA 4412 profile with small angle of attack was obtained in [25].

Results of the developed turbulent flow at $Re = 10^5$ are shown in Fig. 8 for the turbulent kinetic energy, x velocity, streamlines, and contours of the generalized pressure $\overline{p} + \frac{2}{3}\overline{k}$.

However, as one can see from Fig. 7, direct simulation of flow at $Re = 10^4$ does not provide a good match with the inviscid results. This is due to flow detachment and onset of turbulent structures. In Fig. 9 one can see isolines of vorticity for four differents instants in cycle which represent the wide recirculation zone with vortex shedding from the trailing edge of the blade. The whole flow can be considered potential flow for this relatively high-Reynolds-number $Re = 10^4$ only outside this zone.

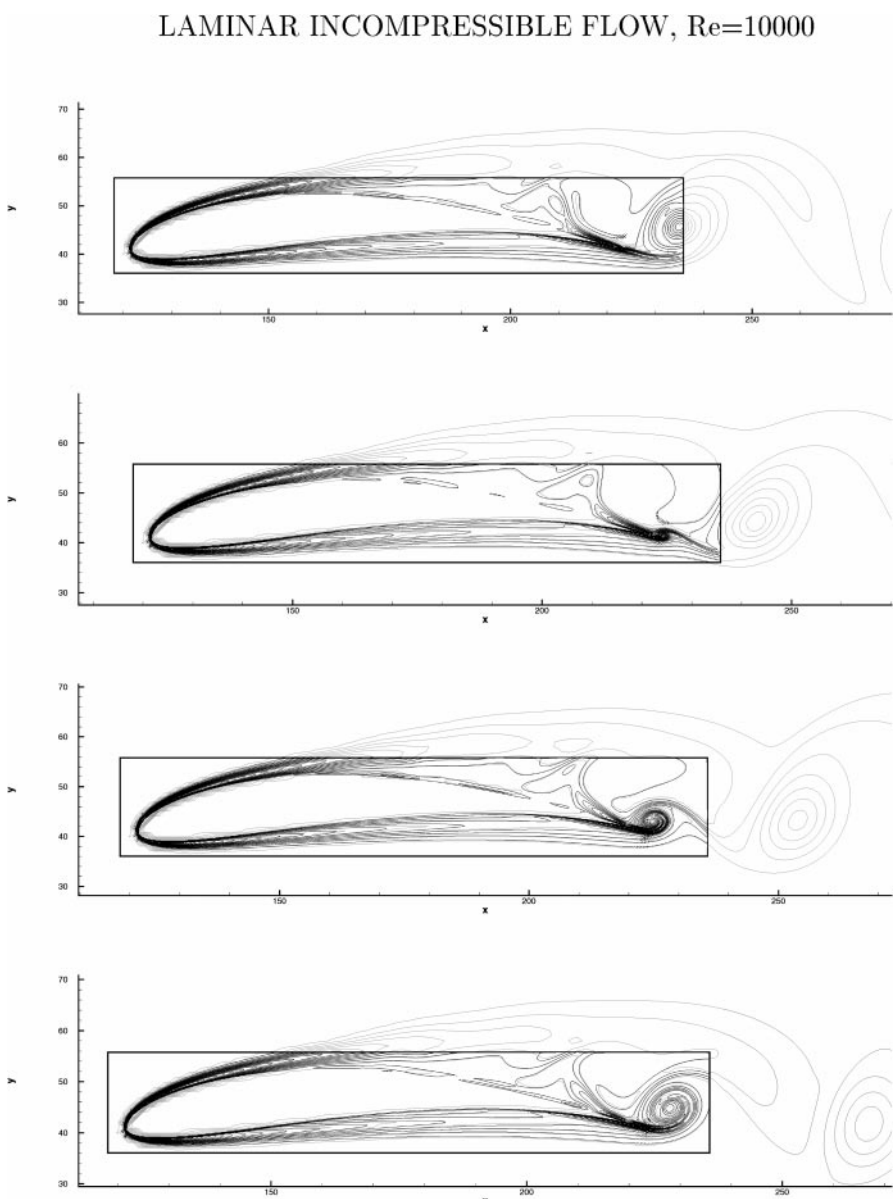

FIG. 9. Vortex shedding from the trailing edge of the blade at $Re = 10^4$, $\alpha = 16^\circ$ at four different instants in the cycle.

CONCLUSIONS

The viability of multiscale LBE schemes for the numerical simulation of turbulent flows in complex curvilinear geometry has been discussed. The main progress is connected with the extension of boundary-fitting formulas on wall function formulations. Decoupling of the numerical mesh and the surface lying inside the logarithmic part of turbulent boundary layer on which boundary-fitting formulas are applied enables the efficient computation of turbulent flows such as two-dimensional flows in an axial compressor cascade, without loosing the simplicity of Cartesian grids. The multiscale LBGK code is clearly more complicated than standard LBGK scheme, but still simpler than state-of-the-art computational fluid dynamic codes with unstructured and locally refined mesh capabilities. Although a detailed head-on comparison on specific benchmark calculations remains to be done, preliminary data indicate comparable performances on serial computers. The great amenability to parallel computing of LBGK schemes, which is to a large extent preserved in the multiscale version, is expected to provide an asset for future LBGK applications to turbulent flows in complex geometries.

REFERENCES

1. G. McNamara and G. Zanetti, Use of the Boltzmann equation to simulate lattice-gas automata, *Phys. Rev. Lett.* **61**, 2332 (1988).
2. F. Higuera, S. Succi, and R. Benzi, Lattice gas dynamics with enhanced collisions, *Europhys. Lett.* **9**, 345 (1989).
3. Y. H. Qian, D. d'Humieres, and P. Lallemand, Lattice BGK models for Navier–Stokes equation, *Europhys. Lett.* **17**(6), 479 (1992).
4. R. Benzi, S. Succi, and M. Vergassola, The lattice Boltzmann equation: Theory and applications, *Phys. Rep.* **222**(3), 145 (1992).
5. S. Chen, Z. Wang, X. Shan, and G. D. Doolen, Lattice Boltzmann computational fluid dynamics in three dimensions, *J. Stat. Phys.* **68**, 379 (1992).
6. S. Succi, G. Amati, and R. Benzi, Challenges in lattice Boltzmann computing, *J. Stat. Phys.* **81**, 5 (1995).
7. G. Amati, S. Succi, and R. Benzi, Turbulent channel flow simulation using a coarse-grained extension of the lattice Boltzmann method, *Fluid Dyn. Res.* **19**, 289 (1997).
8. F. Nannelli and S. Succi, The lattice Boltzmann equation on irregular lattices, *J. Stat. Phys.* **68**(3/4), 401 (1992).
9. X. He, L.-S. Luo, and M. Dembo, Some progress in Lattice Boltzmann method. Part 1. Nonuniform mesh grids, *J. Comput. Phys.* **129**, 357 (1996).
10. O. Filippova and D. Hänel, Boundary-fitting and local grid refinement for lattice-BGK models, *Int. J. Mod. Phys. C* **9**(8), 1271 (1998).
11. A. J. C. Ladd, Numerical simulations of particulate suspensions via a discretized Boltzmann equation. Part 1. Theoretical foundation. *J. Fluid Mech.* **271**, 285 (1994).
12. O. Filippova and D. Hänel, Lattice-BGK model for low Mach number combustion, *Int. J. Mod. Phys. C* **9**(8), 1439 (1998).
13. O. Filippova and D. Hänel, A novel lattice-BGK approach for low Mach number combustion, *J. Comput. Phys.* **158**, 139 (2000).
14. O. Filippova and D. Hänel, Grid refinement for lattice-BGK models, *J. Comput. Phys.* **147**, 219 (1998).
15. F. Mazzocco, C. Arrighetti, G. Bella, L. Spagnoli, and S. Succi, Multiscale lattice Boltzmann schemes: A preliminary application to axial turbomachine flow simulations, *Int. J. Mod. Phys. C* **11**(2), 233 (2000).
16. O. Filippova and D. Hänel, Acceleration of lattice BGK schemes with grid refinement, *J. Comput. Phys.* **165**, 407 (2000).

17. Q. Zou, S. Hou, S. Chen, and G. Doolen, An improved incompressible lattice Boltzmann model for time-independent flows, *J. Stat. Phys.* **81**, 35 (1995).
18. C. Teixeira, Incorporating turbulence models into the lattice-Boltzmann method, *Int. J. Mod. Phys. C* **9**(8), 1159 (1998).
19. S. Succi, H. Chen, C. Teixeira, G. Bella, A. De Maio, and K. Molvig, An integer lattice realization of a Lax scheme for transport processes in multiple component fluid flows, *J. Comp. Phys.* **152**, 493 (1999).
20. B. E. Launder and D. B. Spalding, The numerical computation of turbulent flows, *Comput. Methods Appl. Mech. Eng.* **3**, 269 (1974).
21. V. Yakhot, S. A. Orszag, S. Thangam, T. B. Gatski, and C. G. Speciale, Development of turbulence models for shear flows by a double expansion technique, *Phys. Fluids A* **4**(7), 1510 (1992).
22. J. P. Gostelow, Potential flow through cascades—a comparison between exact and approximate solutions, Aeronautical Research Council, CP 807 (1965).
23. H. Chen, C. Teixeira, and K. Molvig, Realization of fluid boundary conditions via discrete Boltzmann dynamics, *Int. J. Mod. Phys. C* **9**(8), 1281 (1998).
24. S. Hou, J. Sterling, S. Chen, and G. D. Doolen, A lattice Boltzmann subgrid model for high Reynolds number flows, *Field Inst. Comm.* **6**, 151 (1996).
25. E. Baskharone and A. Hamed, A new approach in cascade flow analysis using the finite element method, *AIAA J.* **19**(1), 65 (1981).
26. R. M. Pinkerton, *Calculated and Measured Pressure Distributions over the Midspan Sections of the NACA 4412 Airfoil*, NACA Report 563 (1936).